Nano Research 2016, 9(11): 3478–3493
DOI 10.1007/s12274-016-1225-4
Research Article
ISSN 1998-0124
CN 11-5974/O4

Enhanced CH_4 yield by photocatalytic CO_2 reduction using TiO_2 nanotube arrays grafted with Au, Ru, and ZnPd nanoparticles

Piyush Kar[1,§] (✉), Samira Farsinezhad[1,§], Najia Mahdi[1], Yun Zhang[1], Uchenna Obuekwe[2], Himani Sharma[1], Jing Shen[2], Natalia Semagina[2] (✉), and Karthik Shankar[1,3] (✉)

[1] *Department of Electrical and Computer Engineering, University of Alberta, 9107-116 Street, Edmonton, Alberta, T6G 2V4, Canada*
[2] *Department of Chemical & Materials Engineering, University of Alberta, 9107-116 Street, Edmonton, Alberta, T6G 2V4, Canada*
[3] *NRC National Institute for Nanotechnology, 11421 Saskatchewan Dr. NW, Edmonton, Alberta, T6G 2M9, Canada*
[§] *These authors contributed equally to this work.*

Received: 1 May 2016
Revised: 22 June 2016
Accepted: 21 July 2016

KEYWORDS
metal nanoparticles (NPs),
TiO_2 nanotube arrays (TNAs),
colloidal synthesis,
band bending,
built-in potential,
photocatalytic CO_2 reduction,
semiconductor heterojunctions

ABSTRACT

Metal nanoparticle (NP) co-catalysts on metal oxide semiconductor supports are attracting attention as photocatalysts for a variety of chemical reactions. Related efforts seek to make and use Pt-free catalysts. In this regard, we report here enhanced CH_4 formation rates of 25 and 60 $\mu mol \cdot g^{-1} \cdot h^{-1}$ by photocatalytic CO_2 reduction using hitherto unused ZnPd NPs as well as Au and Ru NPs. The NPs are formed by colloidal synthesis and grafted onto short n-type anatase TiO_2 nanotube arrays (TNAs), grown anodically on transparent glass substrates. The interfacial electric fields in the NP-grafted TiO_2 nanotubes were probed by ultraviolet photoelectron spectroscopy (UPS). Au NP-grafted TiO_2 nanotubes (Au-TNAs) showed no band bending, but a depletion region was detected in Ru NP-grafted TNAs (Ru-TNAs) and an accumulation layer was observed in ZnPd NP-grafted TNAs (ZnPd-TNAs). Temperature programmed desorption (TPD) experiments showed significantly greater CO_2 adsorption on NP-grafted TNAs. TNAs with grafted NPs exhibit broader and more intense UV–visible absorption bands than bare TNAs. We found that CO_2 photoreduction by nanoparticle-grafted TNAs was driven not only by ultraviolet photons with energies greater than the TiO_2 band gap, but also by blue photons close to and below the anatase band edge. The enhanced rate of CO_2 reduction is attributed to superior use of blue photons in the solar spectrum, excellent reactant adsorption, efficient charge transfer to adsorbates, and low recombination losses.

Address correspondence to Piyush Kar, pkar1@ualberta.ca; Natalia Semagina, semagina@ualberta.ca; Karthik Shankar, kshankar@ualberta.ca

1 Introduction

A solution to the problem of managing excessive amounts of CO_2 in the atmosphere is the adoption of sustainable energy sources created using green chemistry. While green chemistry strategies have great economic significance [1], they also are important in addressing issues such as carbon capture and storage and over-reliance on fossil fuel energy. A widely studied application of green chemistry is the reduction of atmospheric CO_2 to value-added chemicals and useful fuels [2]. This approach, which uses atmospheric CO_2 as a reactant, can decrease atmospheric CO_2 levels. In CO_2 photoreduction, synthetic fuels (e.g., CH_4) formed by sunlight driven hydrogenation store solar energy in C–H bonds that become energy sources when combusted.

Conventional methods for transforming CO_2 include biological (e.g., photosynthesis and enzymatic biochemistry), chemical (e.g., amine capture), electrochemical, and photochemical (e.g., sunlight driven photocatalysis) examples. Despite intense research, many problems remain to be solved before photocatalytic CO_2 reduction can become viable on a massive scale. Shortcomings include a lack of ambient stability and reliability in the design of high performance photocatalytic systems, the failure to control complex chemical transformations involving multiple electron transfers, and a lack of mechanistic selectivity resulting in a variety of products (e.g., C_2H_8, HCOOH, HCHO, and CO). Additional impediments are low product yields and adsorption of organic contaminants [3] onto catalyst surfaces, which causes catalyst poisoning and decreases activity. These challenges must be overcome to meet the benchmarks of commercially viable technologies for reduction of CO_2 to CH_4, which is the most completely reduced fuel obtainable from CO_2.

Recent research has emphasized the development of semiconducting nanomaterial platforms [4–12] to efficiently harvest solar light and chemically reduce CO_2 to usable fuels such as CH_3OH and CH_4. A good semiconductor catalyst is characterized by a large light absorption cross-section, effective charge separation and transport properties, favorable electronic energy level alignment, good interfacial charge transfer characteristics, high surface area, favorable surface energetics, and other properties that include stability, resistance to poisoning, cost effectiveness, and non-toxicity. Nanostructuring is commonly used to increase catalytic performance by increasing surface area and improving light absorption through scattering and low minority carrier retrieval distances. Size and structure control of metal nanoparticle (NP) catalysts has been reported to increase their selectivity, activity, and stability in chemical reactions such as hydrogenation, wet oxidation, and ring opening [13–15]. Likewise, when loaded onto TiO_2, bimetallic NPs containing at least one noble metal have been found to be more effective photocatalysts than their monometallic counterparts [16–19].

Typical platforms for CO_2 photoreduction include metallic (e.g., Pd and Au) [11, 20] and bimetallic (e.g., AuCu and CuPt) [21, 22] NPs that act as co-catalysts when grafted onto high surface area semiconducting nanostructures. Good performance has been achieved using one dimensional (1D) semiconducting nanostructures such as nanotubes and nanowires. Among these 1D structures [23], TiO_2 nanotube arrays (TNAs) are a leading platform candidate [6, 24, 25], because of their chemical stability, wall thickness comparable to minority carrier retrieval length, compatibility with a variety of co-catalysts, and tunable size, shape, and semiconducting properties that can be produced by simple procedures [26–28]. TNAs also are effective stand-alone photocatalysts that exhibit improved performance when loaded with co-catalyst NPs (e.g., Cu, Pt, and Pd) [6, 29–33]. Although TNAs with incorporated NPs are established material platforms, various factors limit their CO_2 photoreduction performance. These limitations may be related to the method of loading co-catalysts, the band alignment between catalysts and co-catalysts, and the susceptibility of catalysts and co-catalysts to poisoning.

We recently reported greatly enhanced photocatalytic CO_2 reduction rates using periodically modulated TNAs [6] and TNAs loaded with CuPt NPs [6, 22], where we analyzed the electronic properties of the interface between the TNAs and metal NPs. In this paper, we introduce novel nanoarchitectures comprising metallic NPs grafted onto short, transparent, anodically formed, anatase-type TNAs. The metal NPs were Au, Ru, and ZnPd, which were formed using

solution based colloidal chemistry and grafted onto TNAs. In addition to the enhanced CH_4 yield brought about by NP grafting, all active materials were grown by simple, scalable procedures using non-toxic and environmentally benign precursors. This initial report of bimetallic ZnPd NP grafting onto TNAs is significant in its novelty and superior CH_4 production by photocatalytic CO_2 reduction.

2 Experimental

2.1 Synthesis of Au/Ru/ZnPd NPs grafted onto TNAs

Direct current (DC) magnetron sputtering was used to deposit 500-nm thick titanium (Ti) films on fluorine-doped tin oxide (FTO) glass substrates by techniques described in previous publications [34–36]. The TNAs were grown by electrochemical anodization at an applied voltage of 40 V with an ethylene glycol electrolyte containing 4% deionized (DI) water and 0.3 wt.% NH_4F. Oxygen plasma treatment was applied for 10 min after nanotube growth to clean the surface of adventitious carbon and carbonaceous impurities introduced by anodization. The TNAs were then annealed in an oxygen atmosphere in a tube furnace at 500 ˚C. Poly-(vinylpyrrolidone) (PVP)-stabilized Au, Ru, and ZnPd NPs were synthesized and impregnated onto TNAs with metal loadings of 0.25 mmol Au and Ru and 0.15 mmol ZnPd (1:1 molar ratio) per wafer followed by calcination at 450 ˚C for 1 h in air to remove the organic shell.

Ruthenium(III) nitrosyl nitrate ($Ru(NO)(NO_3)_3$), Alfa Aesar), palladium(II) chloride solution ($PdCl_2$, 5% w/v, Acros), zinc nitrate hexahydrate ($Zn(NO_3)_2{\cdot}6H_2O$, Sigma-Aldrich), hydrogen tetrachloroaurate(III) hydrate ($HAuCl_4{\cdot}3H_2O$, Sigma-Aldrich), PVP (M_W 40,000, Sigma-Aldrich), reagent grade ethanol (95 vol.%, Fisher Scientific), and ethylene glycol (EG, 99.8%, Sigma-Aldrich) were used as received. Milli-Q water was used throughout. Metal nanoparticle decorated TNAs were prepared by impregnating TNAs with colloidal dispersions of the NPs. A summary of the catalysts prepared is presented in Table 1. PVP-stabilized Ru NPs were synthesized by ethylene glycol reduction following procedures described by Semagina et al. [37]. Bimetallic Pd(c)Zn(s) NPs were prepared by Toshima's hydrogen sacrificial technique for a Pd core–Pt shell structure [38]. Pd core NPs were prepared by single step ethanol/water reduction in the presence of PVP (PVP to Pd molar ratio = 20:1) following procedures described in Ref. [37]. The as synthesized monometallic Pd colloid solution (50 mL, 0.05 mmol) was treated with hydrogen gas for 1 h to form Pd hydrides on the surface. The shell precursor solution (50 mL, 0.05 mmol Zn) was prepared and added dropwise to the Pd core colloid solution via syringe pump at a rate of 1 mL·min^{-1} under a hydrogen atmosphere. Free Zn^{2+} ions were reduced by hydrogen atoms on the surface of Pd. The reaction was continued for 2 h to ensure complete reduction of the Zn precursor. The Pd-to-Zn molar ratio was 1:1, and the final PVP-to-metal molar ratio was 10:1. Transparent, homogeneous, dark-brown colloid solutions were obtained without precipitate. Finally, the solvents (ethylene glycol for Ru, ethanol/water for PdZn) of the PVP-stabilized Ru and PdZn colloid solutions were removed by rotary evaporation under vacuum. This was followed by redispersion in water, because water has sufficient surface energy to wet the glass substrates without over-spreading to the edges. The final concentration of the metal nanoparticle solutions was 0.01 M.

Metal NPs were deposited on TNAs by stepwise impregnation. For each deposition, 5 μL of 0.01 M colloid (or precursor) solution was added to the TNAs using a micropipette followed by drying in a 60 ˚C oven. After the desired loadings (0.25 or 0.15 μmol metal) were reached, the catalysts were calcined for 1 h under air in a 450 ˚C furnace to burn off the PVP. To prevent cracking of the glass support, the furnace temperature was increased from 200 to 450 ˚C in steps of 50 ˚C. A 0.01 M Au precursor solution was

Table 1 Summary of synthesized NPs and TiO_2 nanotube-supported catalysts

Catalyst	PVP-to-metal(s) molar ratio	Metal loadings (per TiO_2 sample) (μmol)
Ru	10/1	0.25
Pd(c)Zn(s)	10/1	0.15
Au	—	0.25

prepared by dissolving the appropriate amount of $HAuCl_4 \cdot 3H_2O$ in Milli-Q water. The Au-TiO_2 catalyst was prepared by stepwise impregnation of the TNA with 0.25 μmol Au precursors as described above.

2.2 Material characterization

Field emission scanning electron microscopy (FESEM, Hitachi-NB5000) was used to characterize the morphology of the NP-grafted nanotubes. Phase characterization was conducted by glancing angle X-ray diffraction (XRD) on a Bruker D8 Discover instrument with a sealed Cu tube X-ray source. Ultraviolet visible (UV–vis) spectroscopy (Perkin-Elmer) was used to obtain absorbance spectra of the nanostructures. X-ray photoelectron spectroscopy (XPS) measurements to identify elemental composition and chemical bonding were carried out using an Al Kα source at 1,486.6 eV (Axis-Ultra, Kratos Analytical) under ultrahigh vacuum (UHV, ~10^{-8} Torr). Ultraviolet photoelectron (UPS) spectroscopy was used to obtain work functions and valence band maxima with a 21.21 eV He lamp source.

CHNS analysis was conducted to quantify the carbon content of the synthesized catalysts. Samples were burned at 850 ℃ to detect emitted carbon. CHNS analysis was performed before testing catalysts for CO_2 reduction. Catalysts were pre-calcined for 1 h at 450 ℃ followed by reduction in H_2 at 350 ℃ to duplicate the procedure before CO_2 reduction. After reduction, Ar gas was introduced for 1 h at 450 ℃ to clean the surfaces. CHNS analysis demonstrated that PVP was completely removed by the thermal treatment. Therefore, our metal-NP grafted TNA catalysts did not contribute any carbon to the CO_2 reduction reactions. Au, Ru, and ZnPd catalysts were prepared and deposited on TiO_2 powders for CO and CO_2 temperature programmed desorption (TPD) experiments. The metal loadings were 0.5 wt.%.

The photoreduction of CO_2 to CH_4 was carried out in a stainless steel reaction chamber with water droplets (5 μL, 1 mm diameter). Simulated sunlight was provided by a Newport Instruments AM 1.5 solar simulator equipped with Class A filters. Gas chromatography (GC) was carried out with a Varian Star (Varian, CA, USA) instrument equipped with a Porapak QS column (366 cm long, 3.2 mm o.d., 2 mm i.d.). Thermal conductivity detector (TCD) and flame ionization detector (FID) detectors were employed. The detector temperatures were 180 and 250 ℃ for TCD and FID, respectively. The column temperature was 70 ℃; He was the carrier gas. Products were directed into the gas chromatograph at the end of each run via a gas sampling loop connected to the reactor. The analysis was calibrated with gas samples containing known amounts of methane. The elution order and retention times of the eluents on Porapak Q are provided in Ref. [39]. The peak corresponding to methane appeared at ~0.9 min, while the peak due to air appeared at ~0.6 min following injection.

3 Results and discussion

Figure 1(a) illustrates the one-pot colloidal synthesis used to form the metal NPs. It is a well-established technique employing molecular precursors in conjunction with suitable capping agents to control size, shape, and composition. The schematic depicts Pt NP formation, but a similar process is used to generate other mono- and bimetallic NPs. Although Pt NPs have been successfully employed as co-catalysts and promoters in CO_2 photoreduction [19, 40], we sought alternatives to Pt due to its high cost and vulnerability to poisoning by CO, sulfur, and other chemicals

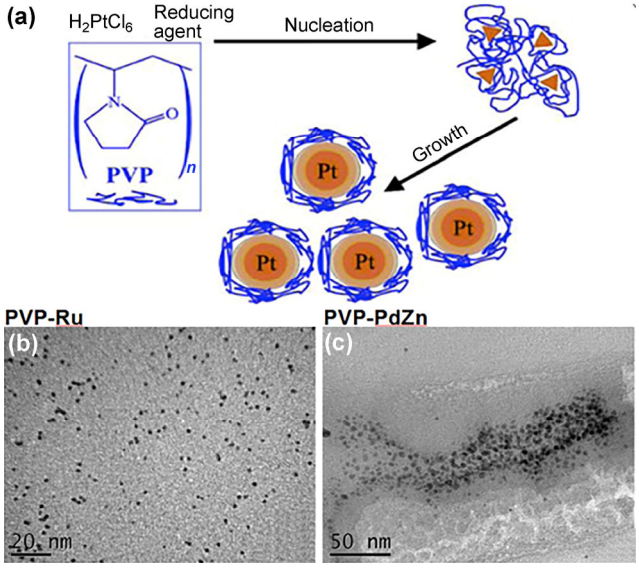

Figure 1 (a) Schematic of the colloidal synthesis of metal nanoparticles using metal-organic precursors and PVP as capping agent. TEM images of PVP-stabilized Ru (b) and ZnPd (c) NPs. Reproduced with permission from Ref. [58], © Springer 2008.

found in flue gases and other sources of CO_2. As shown in Figs. 1(b) and 1(c), we used PVP as the capping agent to stabilize metal NPs for relatively long periods of time (several months). Metal NP size is profoundly important in photocatalysis due to its influence on electron–phonon couplings, lattice strain, work function, band-structure, and the proportion of edge to terrace atoms, which conveys different sorption properties and reactivities [41–44].

3.1 Characterization of Au, Ru, and ZnPd NPs loaded onto TNAs

Figures 2(a)(1), 2(b)(1), and 2(c)(1) contain FESEM images showing NPs of ZnPd, Ru, and Au respectively, decorating the upper surface of TNAs. Low magnification high-resolution transmission electron microscopy (HRTEM) images in Figs. 2(a)(2), 2(b)(2), and 2(c)(2) demonstrate that the metal NPs are grafted onto the walls of the nanotubes. Additional HRTEM images of Au NPs grafted onto the walls of TNAs are shown in Fig. S2 (in the Electronic Supplementary Material (ESM)). High magnification HRTEM images in Figs. 2(a)(3), 2(b)(3), and 2(c)(3) indicate that the NPs are mostly spherical in shape. The electron diffraction patterns in Figs. 2(a)(4), 2(b)(4), and 2(c)(4) depict the prominent crystals planes of the metal NP-grafted TNAs. Anatase crystallinity was confirmed for the TNAs. The lattice spacings in the HRTEM images, which are shown in the insets of Figs. 2(a)(3), 2(b)(3), and 2(c)(3), match the crystal phase information of the electron diffraction patterns. Au, Ru, and ZnPd were determined to be metallic based on JCPDS card nos. 03-065-2870, 03-065-7646, and 03-065-3358/6174, respectively. ZnPd was a mixture of monometallic phases and not an alloy.

The XRD patterns of Au, Ru, and ZnPd NPs on TNAs are shown in Fig. 3(a). Peaks located at 38.85°, 44.45°, and 66.4° denote the (111), (200), and (220) planes in Au NPs (JCPDS card no. 4-784), respectively. Ru TNAs exhibit an intense peak at 44°, which indicates the predominance of Ru (101) in Ru NPs (JCPDS card no. 06-0663). Ru TNAs also show a smaller peak at 42.08° for Ru (002) and a peak at 58.42°, which originates from the Ru (002) plane of the Ru NPs (JCPDS card no. 06-0663). Peaks specific to ZnPd (JCPDS card no. 65-0190) are observed in the XRD patterns of ZnPd

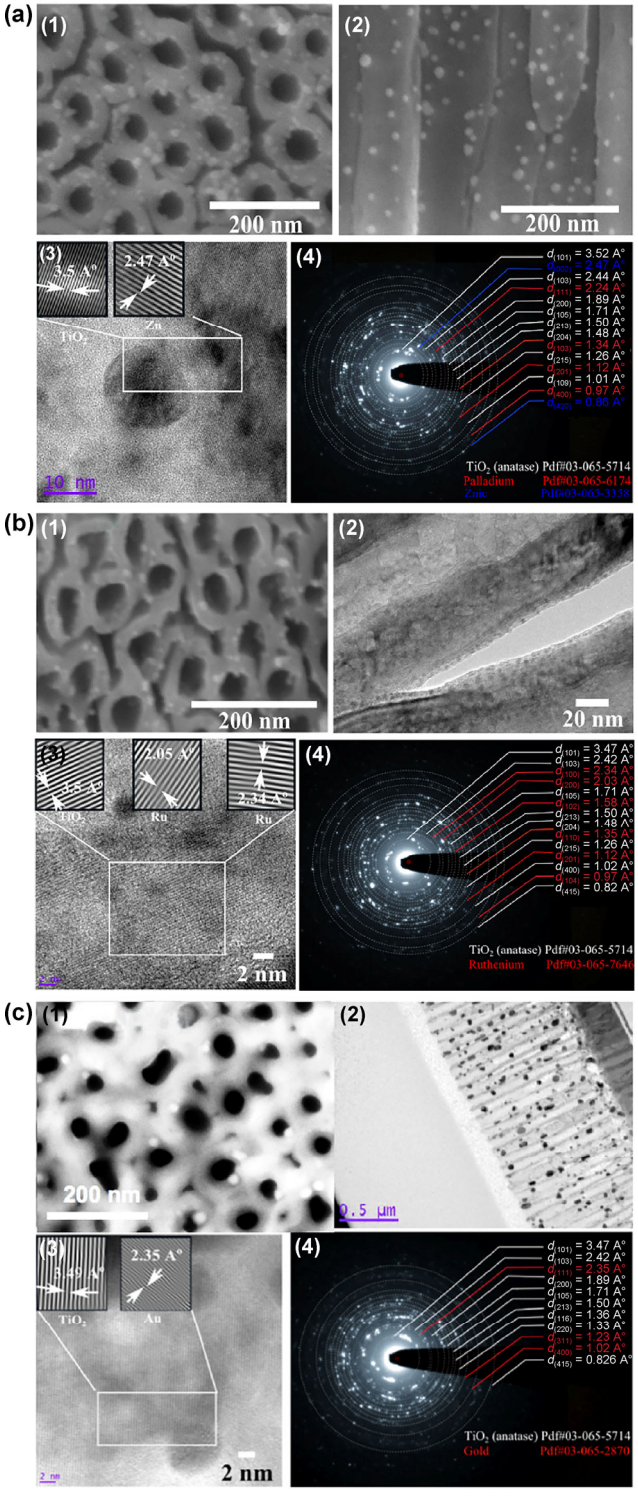

Figure 2 (1) FESEM images, (2) low magnification HRTEM images, (3) high resolution HRTEM images, and (4) electron diffraction patterns of TNAs grafted with ZnPd (a), Ru (b), and Au (c) nanoparticles.

TNAs at 41.46° for the ZnPd (101) plane and at 44.85° for the ZnPd (110) plane (JCPDS card no. 46-1043).

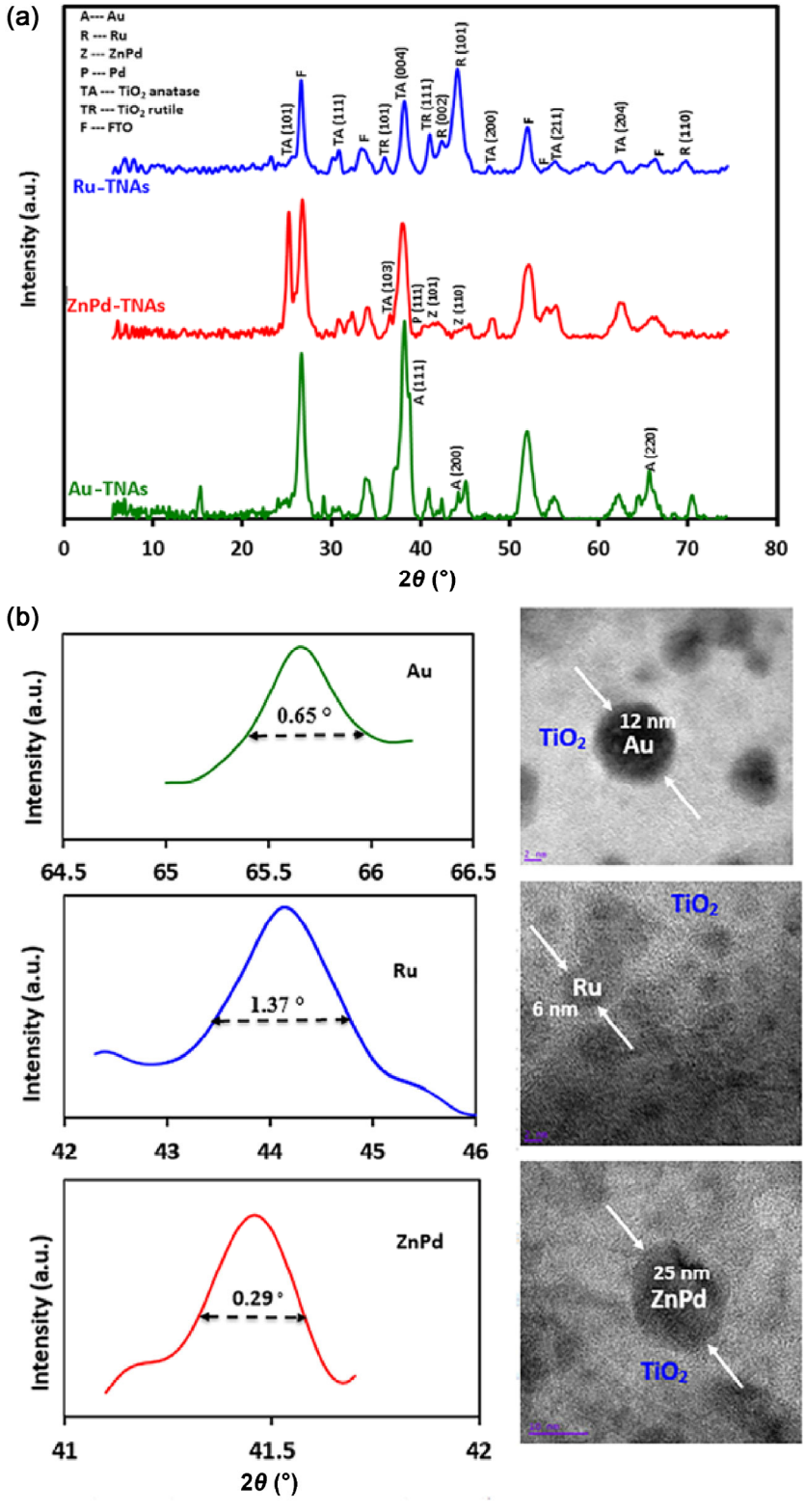

Figure 3 (a) XRD patterns of Au, Ru, and ZnPd nanoparticles on TNAs, and (b) XRD plots showing the FWHM for Au, Ru, and ZnPd nanoparticles on TNAs (left) and TEM images (right) of the nanoparticles illustrating their particle sizes. Nanoparticle size was calculated by Scherrer's equation, which defines particle size as $K\lambda/\beta\cos\theta$, where K is a dimensional shape factor equal to 0.9, λ is the X-ray wavelength (i.e., 0.154 nm), β is the FWHM, and θ is the Bragg angle. The Scherrer equation yields particle sizes of 12.8, 6.0, and 24 nm for the Au, Ru, and ZnPd nanoparticles, respectively.

The remainder of the peaks belong to the anatase of the TNAs (JCPDS card no. 04-001-7641) and to the FTO substrate (JCPDS card no. 41–1445). Although anatase is the dominant phase in the TiO_2, a small quantity of rutile also is observed in the Ru and ZnPd TNAs. The rutile phase (JCPDS card no. 21-1276) may form in the barrier layer of the TNAs near the interface with the FTO substrate, which possesses a tetragonal crystal structure and rutile-type grain orientation. The left side of Fig. 3(b) shows the full widths at half maximum (FWHM) of the XRD peaks that were used to calculate NP size by Scherrer's equation. The Au, Ru, and ZnPd NP sizes are ca. 6.0, 12.8, and 25.0 nm, respectively. The TEM images (Fig. 3(b), right) confirm the calculated sizes.

The size of metal NPs affects photocatalytic performance through factors such as surface energetics, light absorption characteristics, crystalline phase content, and interfacial properties. For example, Ru NPs less than 3 nm in size adopt a hexagonal close packed (HCP) structure, whereas larger NPs exhibit a combination of face centered cubic (FCC) and HCP phases [45], which enhances photocatalytic activity [45, 46]. The average size of our Ru NPs was about 6 nm. This may indicate a mixed phase content, although only the HCP phase was detected in the electron diffraction pattern. The Au NPs adopt the FCC structure, which is evident from the observation of Au (111) planes in the TEM (Fig. 2(c)(4)) and XRD (Fig. 3(a)) data.

Although strategies have been adopted to mediate catalysis by tuning Au NP size to achieve localized surface plasmon resonance (LSPR) [47], our reasoning for the size dependence of catalytic activity is in line with literature reports [48, 49]. These suggest that smaller (3 to 30 nm) Au NPs exhibit greater catalytic activity and that no distinct LSPR peaks are observed due to energy level hybridization of the NPs and support. There are very few reports of ZnPd NP catalysis. However, the 25-nm particle size of our ZnPd NPs matches that in reports [50, 51] where these NPs were used as catalysts.

Transparent TNAs were used to facilitate observation of the effects of metal nanoparticle loading on the optical properties of the nanotubes. The UV–vis spectra in Fig. 4 show a red-shifted absorption edge with a strong sub-bandgap absorption for TNAs grafted with

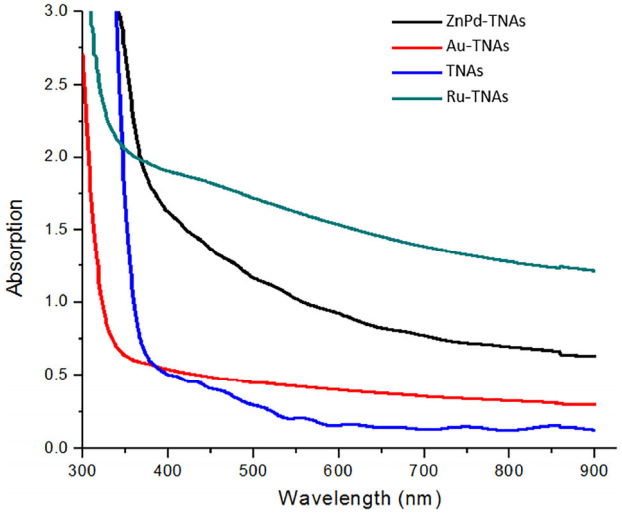

Figure 4 UV–vis spectra of Au, Ru, and ZnPd NP-TNAs.

ZnPd NPs compared to bare TNAs. TNAs with Ru NPs exhibit a strong sub-bandgap absorption and a shoulder at ca. 500 nm suggestive of a secondary absorption edge. TNAs grafted with Au NPs exhibit a broad, weak, featureless absorption in the visible region.

High resolution core XPS scans are shown in Figs. 5(a)–5(f). Au $4f_{7/2}$ and $4f_{5/2}$ binding energies of 84.4 and 88 eV, respectively, are observed in the XPS spectrum, which confirms the presence of Au NPs with a valence state of zero [48, 52–54]. High resolution XPS scans of Ru-TNAs (Fig. 5(b)) show Ru $3d_{5/2}$ and $3d_{3/2}$ peaks at 281 and 284 eV, respectively, which are attributed to metallic Ru [55]. ZnPd NPs exhibit metallic Pd $3d_{5/2}$ and $3d_{3/2}$ peaks (Fig. 5(c)) at 340.5 and 335 eV, respectively [56]. Peaks at 1,022 and 1,045 eV are indicative of Zn^{2+} (Fig. 5(d)) [57]. The same Zn oxidation state in ZnPd has been reported elsewhere [58]. The XPS data show the presence of 63.33% Zn and 36.67% Pd in the ZnPd nanoparticles. Oxygen 1*s* spectra contain contributions at 530.1 and 532.3 eV. The main peak (dashed curve, Fig. 5(e)) at 530.1 eV corresponds to the lattice oxygen in TiO_2, while the smaller peak (dashed curve, Fig. 5(e)) at 532.3 eV indicates surface bound oxygen. Binding energies of 459 and 464.8 eV for Ti 2p (Figs. 5(f)–5(h)) confirm the presence of Ti^{4+} [59–61] in Au, Ru, and ZnPd TNAs. Ti 2p peaks near 461.5 eV, which are present only in Ru- and ZnPd-TNAs (Figs. 5(g) and 5(h)), confirm the presence Ti^{2+} in these samples [62]. The peak near 456.5 eV in the ZnPd-TNAs (Fig. 5(h)) confirms presence of Ti^{3+} [63].

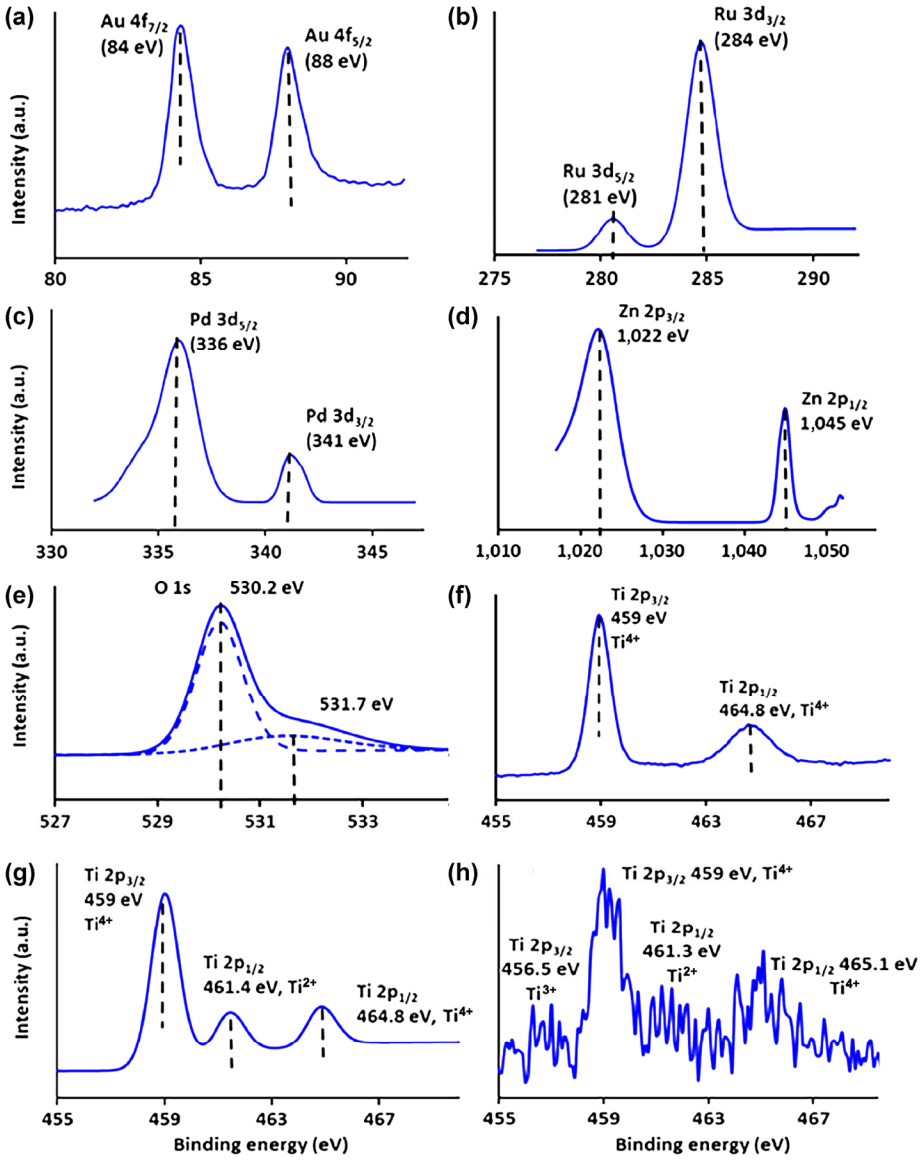

Figure 5 High resolution core XPS spectra of Au-, Ru-, and ZnPd-TNAs. (a) Au 4f in Au-TNAs, (b) Ru 3d in Ru-TNAs, (c) Pd 3d in ZnPd-TNAs, (d) Zn 2p in ZnPd-TNAs, (e) O 1s in Au-TNAs (the O 1s spectra of Ru- and ZnPd-TNAs are identical), (f) Ti 2p in Au-TNAs, (g) Ti 2p in Ru-TNAs, and (h) Ti 2p in ZnPd-TNAs.

The UPS work functions of Au-TNA, Ru-TNA and ZnPd-TNA (Fig. 6(a)) equal 4.50, 4.66, and 3.81 eV, respectively. UPS high binding energy cut-off spectra (Fig. 6(b)) were used to determine the positions of the valence band maxima, which were found at 3.20, 2.75, and 2.97 eV, in Au-TNA, Ru-TNA, and ZnPd-TNA, respectively. Figures 6(a) and 6(b) insets show magnified views of how the values were obtained. Using these data, band bending at the NP-TNA interface is illustrated by the diagrams in Fig. 6(c). An important result derived from the UPS spectra is that upward band bending occurs in TNAs in contact with Ru NPs and downward band bending occurs in TNAs in contact with ZnPd NPs.

3.2 Interfacial electric field between Au, Ru, and ZnPd NPs and TNAs

Considering the range of energy levels commonly observed in TiO_2, band bending in n-type anatase is confirmed by the following conditions: valence band maxima at less than 2.8 eV or more than 3.2 eV away from the Fermi level (E_F) and significant shifts in the

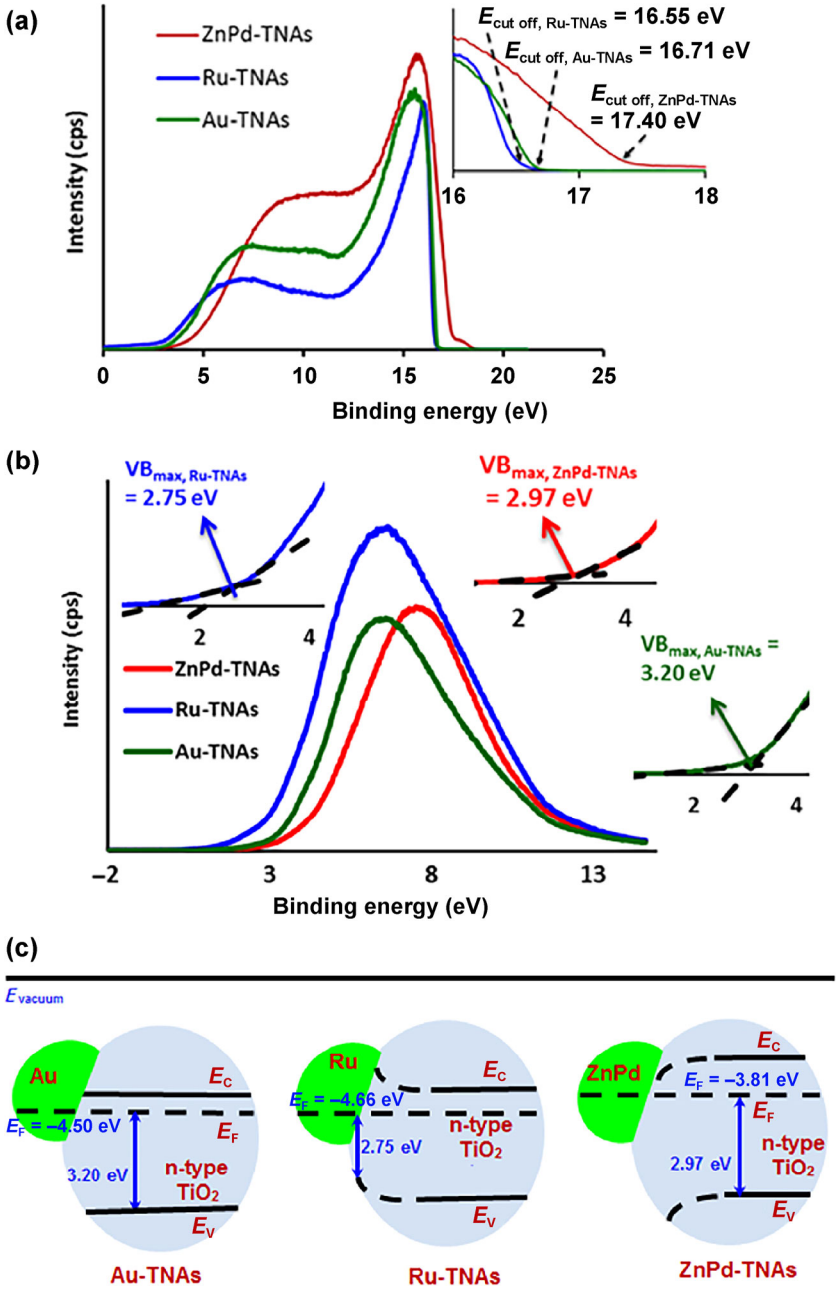

Figure 6 (a) UPS work function spectra for Au-, Ru-, and ZnPd-TNAs; details of the analysis are shown in the insets. (b) UPS valence band spectra showing valence band maxima in Au-TNAs at 3.20 eV, Ru-TNAs at 2.75 eV, and ZnPd- TNAs at 2.97 eV. The work function (wf) was calculated from the expression, wf = 21.21 – $E_{cut\text{-}off}$, where the 21.21 eV is energy of the incident He laser and $E_{cut\text{-}off}$ is the cut-off energy. (c) Illustration of the Fermi energy levels and valence band maxima of Au-, Ru-, and ZnPd- TNAs, as derived from the UPS work function and valence spectra and the band bending characteristics of Au-, Ru-, and ZnPd-TNAs.

core level Ti 2p spectra as indicated by detection of Ti^{3+} and/or work function values less than 4.2 eV or more than 4.5 eV. Shifts in the core level Ti 2p XPS spectra are indicated by the detection of Ti^{3+} and Ti^{2+}, which are not observed in Au-TNAs (Fig. 5(f)), but are observed in Ru- and ZnPd-TNAs (Figs. 5(g) and 5(h)). Core-level Ti 2p shifts can be absent even in the presence of an interfacial electric field, if the loading density of the NPs is low and the width of the resulting depletion region is insufficient to fully deplete the

TiO_2 surface. Considering the lack of a shift in the core level Ti 2p XPS, the position of the Au-TNA valence band maximum at 3.2 eV below the Fermi level (fairly typical for heavily n-doped TiO_2), and a work function of 4.5 eV (within the range of values exhibited by anatase surfaces in high vacuum), we visualize no band bending for Au-TNAs. On the other hand, observation of a valence band maximum at 2.75 eV below the E_F and a work function of 4.66 eV is consistent with upward band bending in Ru-TNAs as shown in Fig. 6(c). Therefore, on the basis of the UPS work function data, grafted Ru NPs form a Schottky type contact with n-type TiO_2 [22]. The work function of ZnPd-TNAs was 3.81 eV, which is significantly less than that of bare, transparent TNAs (≥4.23 eV) [22]. Therefore, downward band bending (accumulation) is visualized for TNAs in contact with ZnPd NPs, which also implies the formation of an ohmic contact between the ZnPd NPs and the TNA. Under illumination, such an interfacial electric field would facilitate transfer of photogenerated electrons from the conduction band of TiO_2 to the ZnPd NPs [22].

3.3 Mechanism of CH_4 production

Activation of CO_2 is a necessary part of the multistep CO_2 reduction process. The activation may take place by absorption of CO_2 onto noble metal NPs [12]. CO_2 can also be activated by adsorption at oxygen vacancy defect sites (such as Ti^{3+} and Ti^{2+}) on TiO_2 surfaces or at photoexcited electron–hole centers in TNAs [64]. During CO_2 activation, conversion of adsorbed CO_2 to a partially charged $CO_2{\cdot}^{\delta-}$ type anionic radical is possible [12, 64–66]. This partially charged radical anion is bent and significantly more reactive than linear CO_2.

One pathway for CH_4 formation is carbene pathway. Following conversion of $CO_2{\cdot}^{\delta-}$ to CO, the carbene pathway proceeds by adsorption of CO onto TiO_2, whereupon it accepts electrons to form a carbon radical (i.e., ·C). Hydrogenation of the carbon radical occurs in presence of electrons from TiO_2 and protons to form ·CH, $\cdot CH_2$, and $\cdot CH_3$ as intermediates and yields CH_4 as the final product [12]. The carbene pathway enhances the selectivity of CH_4 formation, because the reactive nature of the intermediates [67–69] results in rapid hydrogenation.

The carbene pathway is the presumed mechanism of $CO_2{\cdot}^{\delta-}$ to CH_4 conversion in Au- and Ru-TNAS, because depletion layer formation in Ru-TNAs and charge separation in Au-TNAs lead to electron enrichment of the TiO_2 surfaces. Protons are produced by water oxidation at the valence band of TiO_2 in Au-TNAs. In Ru-TNAs, proton generation is driven by water oxidation at the hole-rich Ru NPs. Another mechanism of CH_4 production is the formaldehyde pathway, which involves formation of CH_2O, HCOOH, and CH_3OH as intermediates and CH_4 as the final product [12]. We consider the formaldehyde pathway to be operative in ZnPd-TNAs based on the formation of an accumulation layer, whereby the electron deficient TiO_2 surface cannot support electron donation to CO to form the carbon radical that initiates the carbene pathway. However, ZnPd-TNAs can efficiently reduce $CO_2{\cdot}^{\delta-}$ by electron donation from ZnPd NPs accompanied by donation of protons generated at the hole-rich TiO_2 conduction band to produce CH_4 by the formaldehyde pathway.

3.4 CH_4 yields

The CH_4 yields obtained by gas chromatography were 3.45, 2.3, and 2.32 $mL{\cdot}g^{-1}{\cdot}h^{-1}$ for the Au-, Ru-, and ZnPd-TNAs, respectively. The yields expressed in units of $\mu mol{\cdot}g^{-1}{\cdot}h^{-1}$ were 58.47, 26.37, and 26.83 $\mu mol{\cdot}g^{-1}{\cdot}h^{-1}$ for Au-, Ru- and ZnPd-TNAs, respectively (details are provided in the ESM). CH_4 productions per unit mass of catalyst were 467.79, 210.96, and 214.65 $\mu mol{\cdot}g^{-1}$ for Au-, Ru-, and ZnPd-TNAs, respectively. The methane yields in $\mu mol{\cdot}g^{-1}$ were obtained by multiplying each CH_4 yield in $\mu mol{\cdot}g^{-1}{\cdot}h^{-1}$ by the catalysis reaction time (i.e., 8 h). The total quantities of CH_4 obtained by multiplying by the mass of each catalyst were 0.59, 0.26, and 0.26 μmol for Au-, Ru-, and ZnPd-TNAs, respectively (details are given in the ESM).

Table 2 compares CH_4 yields in $\mu mol{\cdot}g^{-1}{\cdot}h^{-1}$ of our catalysts with those of similar catalysts under similar reaction conditions. One of the highest yields is the value 2,000 $\mu mol{\cdot}g^{-1}{\cdot}h^{-1}$ reported in Ref. [69], which used Au–Cu alloy NPs as a coating on TiO_2 and involved the use of a greater proportion of Au as

a stand-alone catalyst. However, our CH_4 yields are significant, when it is considered that only small quantities of NPs are incorporated on the TNAs, because of the short length of the TNA walls that are sparsely covered with NPs (Figs. 2(a)(2), 2(b)(2), and 2(c)(2)). The comparison in Table 2 of our CH_4 yields with those obtained using similar catalytic platforms [9, 32, 40, 70–72] indicates that Au, Ru, and ZnPd NP-TNAs clearly meet or exceed current state-of-the-art catalytic benchmarks.

An important aspect of our CH_4 yield results is that minor modifications of the catalysts achieved by varying the aspect ratio of the TNAs and the loading of metal NPs conceivably can increase yields by an order of magnitude or more. The enhancement of CH_4 yields of TNAs grafted with Au, ZnPd, and Pd NPs demonstrates the chemical compatibility of the NPs with the underlying TNA support. CH_4 production using short TNAs loaded with Au, ZnPd, and Ru NPs also exceeded by up to ten times the maximum quantity produced (i.e., 6 $\mu mol \cdot g^{-1} \cdot h^{-1}$) using bare TNAs under identical experimental conditions.

NP co-catalysts are critical to CH_4 production as indicated by the TPD data in Fig. 7, which demonstrate that greater amounts of CO_2 are adsorbed on TNAs

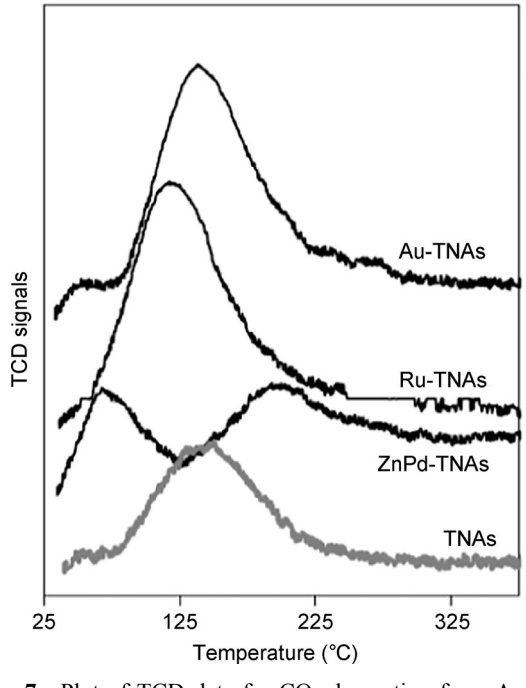

Figure 7 Plot of TCD data for CO_2 desorption from Au-, Ru- and ZnPd-TNAs.

with grafted NPs than on standalone TNAs. Greater CH_4 yields are consistent with a proportionality between yield and the amount of adsorbed CO_2. Excellent transfer of photogenerated charge to surface adsorbates, which is a prerequisite for efficient CO_2 reduction, also is implied. While the chemisorption modes of CO_2 on Ru-grafted, Au-grafted, and bare TNAs are similar and differ only in intensity, ZnPd NP-grafted TNAs exhibit distinctly different CO_2 chemisorption behavior. The desorption peaks at 75 and 187 °C likely are due to sequential release of CO_2 from the Zn and Pd facets of bimetallic ZnPd NPs.

Recent results from our group [36, 73] and others [74–77] point to extremely long lived carrier states in TNA arrays under ambient conditions due to adsorbed oxygen-mediated trapping and a paucity of recombination pathways involving trapped electrons and holes. Because trapped holes and electrons can react directly with adsorbed surface reagents [78, 79], a long carrier recombination lifetime, as manifested by persistent photoconductivity, allows carriers optimum time to participate in chemical reactions and reduce recombination losses. Our GC results from experiments without filters (Figs. S3, S4, and S5 in the ESM) and with UV and blue filters (Figs. S6, S7, and S8 in the ESM) demonstrate the presence of CH_4 as a significant product. Given that the blue filter transmits light between 420 and 480 nm (Fig. S9 in the ESM), it is concluded that, in addition to UV photons, the CO_2 reduction reaction is driven by blue photons with energies close to and below the TiO_2 band gap.

Table 2 CH_4 yields from CO_2 photoreduction using catalytic platforms similar to Au, Ru, and ZnPd loaded onto TNAs

Catalyst	CH_4 yield ($\mu mol \cdot g^{-1} \cdot h^{-1}$)	Refs.
Au-TNAs	58.47	This report
Ru-TNAs	26.37	This report
ZnPd-TNAs	26.83	This report
Au/Pt–TiO_2	114	[71]
$W_{18}O_{49}$	11.31	[80]
Pt–Cu/TiO_2	9.8	[9]
0.5 wt.% Cu/TiO_2–SiO_2	10	[81]
Au-Cu/TiO_2	2,000	[69]

3.5 The issue of carbon contamination

It has been argued in the literature that the source of CH_4 formation is carbon contamination on the surface of TNAs [82]. Contamination may result from any or all of the following: (i) adventitious carbon, (ii) carbon incorporated in TNAs during anodization, and (iii) carbonaceous materials associated with loading of the NPs. This argument is based on the production of CH_4 by direct photoreduction of carbon in presence of water without involvement of CO_2 as a reactant. The argument also applies to the reverse Boudouard reaction, which involves the photoreduction of CO_2 to CO in the presence of surface carbon contaminants that participate in the reaction [83]. We conducted control experiments to verify that CH_4 was indeed produced by CO_2 photoreduction over metal NP-loaded TNAs. These experiments included, but were not limited to the following. (a) A dark experiment in a reactor containing CO_2 gas and a fresh metal-NP decorated nanotube photocatalyst heated to over 80 °C for 8 h. The negligibly small amount of CH_4 produced verifies the importance of light in driving the reaction. (b) An experiment conducted under AM 1.5 illumination in an empty reactor containing CO_2 to assess the possible presence of CH_4 and other hydrocarbons in the CO_2 input stream or reaction chamber. (c) An experiment conducted under AM 1.5 illumination in a reactor containing fresh bare TiO_2 nanotube photocatalyst (without metal NP coating) in the absence of CO_2 to measure the effect of carbon possibly doped into the TNAs. (d) An analysis of CH_4 production as a function of time, which demonstrated that CH_4 production increased steadily throughout exposure to light.

To evaluate the impact of carbon on CH_4 formation, we determined the amount of carbon in the samples by CHNS analysis. For Ru and ZnPd NPs loaded onto TNAs in the as prepared state (after calcination at 450 °C to remove PVP), the contaminant carbon was 0.083 μmol in the Ru-TNA and 0.061 μmol in the ZnPd-TNA. Therefore, if all contaminant carbon in the samples reacted completely to form CH_4, the amount of methane produced would be a small fraction of the total generated by the photocatalysts in this study.

4 Conclusions

The enhanced photocatalytic performance of NP-grafted TNAs suggests the possibility of further increasing photocatalytic yields by controlling and optimizing particle size and by loading onto vertically oriented 1D semiconducting nanostructured platforms. High CH_4 yields were obtained with short TNAs, which provided less surface area for incorporation of NPs. Significantly enhanced CH_4 production rates were observed using Au, Ru, and ZnPd NPs grafted onto short, transparent TNAs compared to the same obtained using bare TNAs under identical reaction conditions. UPS revealed favorable band alignments for water oxidation and CO_2 reduction reactions which are necessary for CH_4 production. The enhanced CH_4 yields are attributed to the high CO_2 adsorption capacity of NP-loaded TNAs and to the favorable interfacial electric field, superior utilization of blue photons, and excellent charge separation and charge transfer properties of the nanomaterial photocatalyst. The simplicity of the procedure for forming TNAs and grafting monodisperse metal NPs facilitates the tuning of nanostructure architectures to further enhance CH_4 yields and provide more efficient CO_2 reduction.

Acknowledgements

All authors thank NSERC and the Canada School of Energy and the Environment for funding support. K. S. thanks NRC-NINT for funding and equipment usage, CFI and Alberta Advanced Education for research infrastructure, and CMC Microsystems for financial assistance with nanofabrication and characterization activities. S. F., H. S. and P. K. acknowledge the staff of the UofA Nanofab and Kai Cui at NRC-NINT for assistance with microscopy. S. F. thanks Alberta Innovates Technology Futures for scholarship support.

Electronic Supplementary Material: Supplementary material (CH_4 yield calculations and supporting data) is available in the online version of this article at http://dx.doi.org/10.1007/s12274-016-1225-4.

References

[1] Mulvihill, M. J.; Beach, E. S.; Zimmerman, J. B.; Anastas, P. T. Green chemistry and green engineering: A framework for sustainable technology development. *Ann. Rev. Environ. Resour.* **2011**, *36*, 271–293.

[2] Leitner, W. Carbon dioxide as a raw material: The synthesis of formic acid and its derivatives from CO_2. *Angew. Chem, Int. Ed.* **1995**, *34*, 2207–2221.

[3] Yui, T.; Kan, A.; Saitoh, C.; Koike, K.; Ibusuki, T.; Ishitani, O. Photochemical reduction of CO_2 using TiO_2: Effects of organic adsorbates on TiO_2 and deposition of Pd onto TiO_2. *ACS Appl. Mater. Interfaces* **2011**, *3*, 2594–2600.

[4] Manzi, A.; Simon, T.; Sonnleitner, C.; Döblinger, M.; Wyrwich, R.; Stern, O.; Stolarczyk, J. K.; Feldmann, J. Light-induced cation exchange for copper sulfide based CO_2 reduction. *J. Am. Chem. Soc.* **2015**, *137*, 14007–14010.

[5] Kar, P.; Farsinezhad, S.; Zhang, X. J.; Shankar, K. Anodic Cu_2S and CuS nanorod and nanowall arrays: Preparation, properties and application in CO_2 photoreduction. *Nanoscale* **2014**, 6, 14305–14318.

[6] Zhang, X. J.; Han, F.; Shi, B.; Farsinezhad, S.; Dechaine, G. P.; Shankar, K. Photocatalytic conversion of diluted CO_2 into light hydrocarbons using periodically modulated multiwalled nanotube arrays. *Angew. Chem.* **2012**, *124*, 12904–12907.

[7] Wang, S. B.; Hou, Y. D.; Wang, X. C. Development of a stable $MnCo_2O_4$ cocatalyst for photocatalytic CO_2 reduction with visible light. *ACS Appl. Mater. Interfaces* **2015**, *7*, 4327–4335.

[8] Wang, S. B.; Wang, X. C. Photocatalytic CO_2 reduction by CdS promoted with a zeolitic imidazolate framework. *Appl. Catal. B: Environ.* **2015**, *162*, 494–500.

[9] Zhai, Q. G.; Xie, S. J.; Fan, W. Q.; Zhang, Q. H.; Wang, Y.; Deng, W. P.; Wang, Y. Photocatalytic conversion of carbon dioxide with water into methane: Platinum and copper(I) oxide co-catalysts with a core–shell structure. *Angew. Chem.* **2013**, *125*, 5888–5891.

[10] Tu, W. G.; Zhou, Y.; Zou, Z. G. Photocatalytic conversion of CO_2 into renewable hydrocarbon fuels: State-of-the-art accomplishment, challenges, and prospects. *Adv. Mater.* **2014**, *26*, 4607–4626.

[11] Marszewski, M.; Cao, S. W.; Yu, J. G.; Jaroniec, M. Semiconductor-based photocatalytic CO_2 conversion. *Mater. Horiz.* **2015**, *2*, 261–278.

[12] Habisreutinger, S. N.; Schmidt-Mende, L.; Stolarczyk, J. K. Photocatalytic reduction of CO_2 on TiO_2 and other semiconductors. *Angew. Chem., Int. Ed.* **2013**, *52*, 7372–7408.

[13] Wettstein, S. G.; Bond, J. Q.; Alonso, D. M.; Pham, H. N.; Datye, A. K.; Dumesic, J. A. RuSn bimetallic catalysts for selective hydrogenation of levulinic acid to γ-valerolactone. *Appl. Catal. B: Environ.* **2012**, *117–118*, 321–329.

[14] Fu, J. L.; Yang, K. X.; Ma, C. J.; Zhang, N. W.; Gai, H. J.; Zheng, J. B.; Chen, B. H. Bimetallic Ru–Cu as a highly active, selective and stable catalyst for catalytic wet oxidation of aqueous ammonia to nitrogen. *Appl. Catal. B: Environ.* **2016**, *184*, 216–222.

[15] Ziaei-azad, H.; Yin, C.-X.; Shen, J.; Hu, Y. F.; Karpuzov, D.; Semagina, N. Size- and structure-controlled mono- and bimetallic Ir–Pd nanoparticles in selective ring opening of indan. *J. Catal.* **2013**, *300*, 113–124.

[16] Zielińska-Jurek, A.; Kowalska, E.; Sobczak, J. W.; Lisowski, W.; Ohtani, B.; Zaleska, A. Preparation and characterization of monometallic (Au) and bimetallic (Ag/Au) modified-titania photocatalysts activated by visible light. *Appl. Catal. B: Environ.* **2011**, *101*, 504–514.

[17] Gallo, A.; Marelli, M.; Psaro, R.; Gombac, V.; Montini, T.; Fornasiero, P.; Pievo, R.; Dal Santo, V. Bimetallic Au–Pt/TiO_2 photocatalysts active under UV-A and simulated sunlight for H_2 production from ethanol. *Green Chem.* **2012**, *14*, 330–333.

[18] Tsukamoto, D.; Shiro, A.; Shiraishi, Y.; Sugano, Y.; Ichikawa, S.; Tanaka, S.; Hirai, T. Photocatalytic H_2O_2 production from ethanol/O_2 system using TiO_2 loaded with Au–Ag bimetallic alloy nanoparticles. *ACS Catal.* **2012**, *2*, 599–603.

[19] Amirsolaimani, B.; Zhang, X. J.; Han, F.; Farsinezhad, S.; Mohammadpour, A.; Dechaine, G.; Shankar, K. Effect of the nature of the metal co-catalyst on CO_2 photoreduction using fast-grown periodically modulated titanium dioxide nanotube arrays (PMTiNTs). *MRS Proc.* **2013**, *1578*, DOI: 10.1557/opl.2013.841.

[20] Feng, S. C.; Wang, M.; Zhou, Y.; Li, P.; Tu, W. G.; Zou, Z. G. Double-shelled plasmonic Ag-TiO_2 hollow spheres toward visible light-active photocatalytic conversion of CO_2 into solar fuel. *APL Mater.* **2015**, *3*, 104416.

[21] Kang, Q.; Wang, T.; Li, P.; Liu, L. Q.; Chang, K.; Li, M.; Ye, J. H. Photocatalytic reduction of carbon dioxide by hydrous hydrazine over Au–Cu alloy nanoparticles supported on $SrTiO_3$/TiO_2 coaxial nanotube arrays. *Angew. Chem.* **2015**, *127*, 855–859.

[22] Farsinezhad, S.; Sharma, H.; Shankar, K. Interfacial band alignment for photocatalytic charge separation in TiO_2 nanotube arrays coated with CuPt nanoparticles. *Phys. Chem. Chem. Phys.* **2015**, *17*, 29723–29733.

[23] Xiao, F. X.; Miao, J. W.; Tao, H. B.; Hung, S. F.; Wang, H. Y.; Yang, H. B.; Chen, J. Z.; Chen, R.; Liu, B. One-dimensional hybrid nanostructures for heterogeneous photocatalysis and photoelectrocatalysis. *Small* **2015**, *11*, 2115–2131.

[24] Varghese, O. K.; Paulose, M.; LaTempa, T. J.; Grimes, C. A. High-rate solar photocatalytic conversion of CO_2 and water vapor to hydrocarbon fuels. *Nano Lett.* **2009**, *9*, 731–737.

[25] Paramasivam, I.; Jha, H.; Liu, N.; Schmuki, P. A review of photocatalysis using self-organized TiO_2 nanotubes and other ordered oxide nanostructures. *Small* **2012**, *8*, 3073–3103.

[26] Chen, X. B.; Mao, S. S. Titanium dioxide nanomaterials: Synthesis, properties, modifications, and applications. *Chem. Rev.* **2007**, *107*, 2891–2959.

[27] Kar, P.; Zhang, Y.; Farsinezhad, S.; Mohammadpour, A.; Wiltshire, B. D.; Sharma, H.; Shankar, K. Rutile phase n- and p-type anodic titania nanotube arrays with square-shaped pore morphologies. *Chem. Commun.* **2015**, *51*, 7816–7819.

[28] Mor, G. K.; Shankar, K.; Paulose, M.; Varghese, O. K.; Grimes, C. A. Enhanced photocleavage of water using titania nanotube arrays. *Nano Lett.* **2005**, *5*, 191–195.

[29] Kočí, K.; Obalová, L.; Matějová, L.; Plachá, D.; Lacný, Z.; Jirkovský, J.; Šolcová, O. Effect of TiO_2 particle size on the photocatalytic reduction of CO_2. *Appl. Catal. B: Environ.* **2009**, *89*, 494–502.

[30] Murugesan, S.; Smith, Y. R.; Subramanian, V. Hydrothermal synthesis of $Bi_{12}TiO_{20}$ nanostrucutures using anodized TiO_2 nanotubes and its application in photovoltaics. *The J. Phys. Chem. Lett.* **2010**, *1*, 1631–1636.

[31] Yu, J. G.; Low, J. X.; Xiao, W.; Zhou, P.; Jaroniec, M. Enhanced photocatalytic CO_2-reduction activity of anatase TiO_2 by coexposed {001} and {101} facets. *J. Am. Chem. Soc.* **2014**, *136*, 8839–8842.

[32] Xie, T.-F.; Wang, D.-J.; Zhu, L.-J.; Li, T.-J.; Xu, Y.-J. Application of surface photovoltage technique in photocatalysis studies on modified TiO_2 photo-catalysts for photo-reduction of CO_2. *Mater. Chem. Phys.* **2001**, *70*, 103–106.

[33] Tseng, I.-H.; Wu, J. C. S.; Chou, H.-Y. Effects of sol–gel procedures on the photocatalysis of Cu/TiO_2 in CO_2 photoreduction. *J. Catal.* **2004**, *221*, 432–440.

[34] Farsinezhad, S.; Mohammadpour, A.; Dalrymple, A. N.; Geisinger, J.; Kar, P.; Brett, M. J.; Shankar, K. Transparent anodic TiO_2 nanotube arrays on plastic substrates for disposable biosensors and flexible electronics. *J. Nanosci. Nanotechnol.* **2013**, *13*, 2885–2891.

[35] Farsinezhad, S.; Dalrymple, A. N.; Shankar, K. Toward single-step anodic fabrication of monodisperse TiO_2 nanotube arrays on non-native substrates. *Phys. Status Solidi (a)* **2014**, *211*, 1113–1121.

[36] Mohammadpour, A.; Kar, P.; Wiltshire, B. D.; Askar, A. M.; Shankar, K. Electron transport, trapping and recombination in anodic TiO_2 nanotube arrays. *Curr. Nanosci.* **2015**, *11*, 593–614.

[37] Shen, J.; Semagina, N. Iridium- and platinum-free ring opening of indan. *ACS Catal.* **2014**, *4*, 268–279.

[38] Wang, Y.; Toshima, N. Preparation of Pd-Pt bimetallic colloids with controllable core/shell structures. *J. Phys. Chem. B* **1997**, *101*, 5301–5306.

[39] Xu, X. J.; Pacey, P. D. Oligomerization and cyclization reactions of acetylene. *Phys. Chem. Chem. Phys.* **2005**, *7*, 326–333.

[40] Wang, W.-N.; An, W.-J.; Ramalingam, B.; Mukherjee, S.; Niedzwiedzki, D. M.; Gangopadhyay, S.; Biswas, P. Size and structure matter: Enhanced CO_2 photoreduction efficiency by size-resolved ultrafine Pt nanoparticles on TiO_2 single crystals. *J. Am. Chem. Soc.* **2012**, *134*, 11276–11281.

[41] Hodak, J. H.; Henglein, A.; Hartland, G. V. Photophysics of nanometer sized metal particles: Electron–phonon coupling and coherent excitation of breathing vibrational modes. *J. Phys. Chem. B* **2000**, *104*, 9954–9965.

[42] Sneed, B. T.; Young, A. P.; Tsung, C.-K. Building up strain in colloidal metal nanoparticle catalysts. *Nanoscale* **2015**, *7*, 12248–12265.

[43] Shen, J.; Yin, X.; Karpuzov, D.; Semagina, N. PVP-stabilized mono- and bimetallic Ru nanoparticles for selective ring opening. *Catal. Sci. Technol.* **2013**, *3*, 208–221.

[44] Ziaei-Azad, H.; Semagina, N. Bimetallic catalysts: Requirements for stabilizing PVP removal depend on the surface composition. *Appl. Catal. A: Gen.* **2014**, *482*, 327–335.

[45] Joo, S. H.; Park, J. Y.; Renzas, J. R.; Butcher, D. R.; Huang, W. Y.; Somorjai, G. A. Size effect of ruthenium nanoparticles in catalytic carbon monoxide oxidation. *Nano Lett.* **2010**, *10*, 2709–2713.

[46] Reyes, P.; König, M. E.; Pecchi, G.; Concha, I.; López Granados, M.; Fierro, J. L. G. o-Xylene hydrogenation on supported ruthenium catalysts. *Catal. Lett.* **1997**, *46*, 71–75.

[47] Qian, K.; Sweeny, B. C.; Johnston-Peck, A. C.; Niu, W. X.; Graham, J. O.; DuChene, J. S.; Qiu, J. J.; Wang, Y.-C.; Engelhard, M. H.; Su, D. et al. Surface plasmon-driven water reduction: Gold nanoparticle size matters. *J. Am. Chem. Soc.* **2014**, *136*, 9842–9845.

[48] Murdoch, M.; Waterhouse, G. I. N.; Nadeem, M. A.; Metson, J. B.; Keane, M. A.; Howe, R. F.; Llorca, J.; Idriss, H. The effect of gold loading and particle size on photocatalytic hydrogen production from ethanol over Au/TiO_2 nanoparticles. *Nat. Chem.* **2011**, *3*, 489–492.

[49] Rajan, A.; MeenaKumari, M.; Philip, D. Shape tailored green synthesis and catalytic properties of gold nanocrystals. *Spectrochim. Acta A: Mol. Biomol. Spectrosc.* **2014**, *118*, 793–799.

[50] Dagle, R. A.; Chin, Y.-H.; Wang, Y. The effects of PdZn crystallite size on methanol steam reforming. *Top. Catal.* **2007**, *46*, 358–362.

[51] Karim, A.; Conant, T.; Datye, A. The role of PdZn alloy formation and particle size on the selectivity for steam reforming of methanol. *J. Catal.* **2006**, *243*, 420–427.

[52] Kruse, N.; Chenakin, S. XPS characterization of Au/TiO_2 catalysts: Binding energy assessment and irradiation effects. *Appl. Catal. A: Gen.* **2011**, *391*, 367–376.

[53] Sobczak, J. W.; Andreeva, D. XPS study of Au/TiO_2 catalytic systems. *Stud. Surf. Sci. Catal.* **2000**, *130*, 3303–3308.

[54] Lee, S.; Fan, C. Y.; Wu, T. P.; Anderson, S. L. Agglomeration, support effects, and CO adsorption on Au/TiO_2 (110) prepared by ion beam deposition. *Surf. Sci.* **2005**, *578*, 5–19.

[55] Elmasides, C.; Kondarides, D. I.; Grünert, W.; Verykios, X. E. XPS and FTIR study of Ru/Al_2O_3 and Ru/TiO_2 catalysts: Reduction characteristics and interaction with a methane-oxygen mixture. *J. Phys. Chem. B* **1999**, *103*, 5227–5239.

[56] Semagina, N.; Renken, A.; Laub, D.; Kiwi-Minsker, L. Synthesis of monodispersed palladium nanoparticles to study structure sensitivity of solvent-free selective hydrogenation of 2-methyl-3-butyn-2-ol. *J. Catal.* **2007**, *246*, 308–314.

[57] Morozov, I. G.; Belousova, O. V.; Ortega, D.; Mafina, M.-K.; Kuznetcov, M. V. Structural, optical, XPS and magnetic properties of Zn particles capped by ZnO nanoparticles. *J. Alloys Compd.* **2015**, *633*, 237–245.

[58] Armbrüster, M.; Behrens, M.; Föttinger, K.; Friedrich, M.; Gaudry, É.; Matam, S. K.; Sharma, H. R. The intermetallic compound ZnPd and its role in methanol steam reforming. *Catal. Rev.* **2013**, *55*, 289–367.

[59] Grimes, C. A.; Mor, G. K. Material properties of TiO_2 nanotube arrays: Structural, elemental, mechanical, optical and electrical. In *TiO_2 Nanotube Arrays*; Springer: New York, 2009; pp 67–113.

[60] Sexton, B. A.; Hughes, A. E.; Foger, K. XPS investigation of strong metal-support interactions on Group IIIa–Va oxides. *J. Catal.* **1982**, *77*, 85–93.

[61] Shpiro, E. S.; Dysenbina, B. B.; Tkachenko, O. P.; Antoshin, G. V.; Minachev, K. M. Strong metal-support interaction: The role of electronic and geometric factors in real MeTiO_2 catalysts. *J. Catal.* **1988**, *110*, 262–274.

[62] Lee, K. B.; Lee, K. H.; Cha, J. O.; Ahn, J. S. Ti–O binding states of resistive switching TiO_2 thin films prepared by reactive magnetron sputtering. *J. Korean Phys. Soc.* **2008**, *53*, 1996–2001.

[63] Sasan, K.; Zuo, F.; Wang, Y.; Feng, P. Y. Self-doped Ti^{3+}–TiO_2 as a photocatalyst for the reduction of CO_2 into a hydrocarbon fuel under visible light irradiation. *Nanoscale* **2015**, *7*, 13369–13372.

[64] Indrakanti, V. P.; Kubicki, J. D.; Schobert, H. H. Photoinduced activation of CO_2 on Ti-based heterogeneous catalysts: Current state, chemical physics-based insights and outlook. *Energy Environ. Sci.* **2009**, *2*, 745–758.

[65] Tanaka, K.; Miyahara, K.; Toyoshima, I. Adsorption of carbon dioxide on titanium dioxide and platinum/titanium dioxide studied by X-ray photoelectron spectroscopy and Auger electron spectroscopy. *J. Phys. Chem.* **1984**, *88*, 3504–3508.

[66] Rasko, J.; Solymosi, F. Infrared spectroscopic study of the photoinduced activation of CO_2 on TiO_2 and Rh/TiO_2 catalysts. *J. Phys. Chem.* **1994**, *98*, 7147–7152.

[67] Kaneco, S.; Ohta, K.; Shimizu, Y.; Mizuno, T. Photocatalytic reduction of high pressure carbon dioxide using TiO_2 powders. In *Recent Research Developments in Photochemistry and Photobiology*; 1998; pp 91–100.

[68] Dey, G. R. Chemical reduction of CO_2 to different products during photo catalytic reaction on TiO_2 under diverse conditions: An overview. *J. Nat. Gas Chem.* **2007**, *16*, 217–226.

[69] Neaţu, Ş; Maciá-Agulló, J. A.; Concepción, P.; Garcia, H. Gold–copper nanoalloys supported on TiO_2 as photocatalysts for CO_2 reduction by water. *J. Am. Chem. Soc.* **2014**, *136*, 15969–15976.

[70] Liu, L. J.; Gao, F.; Zhao, H. L.; Li, Y. Tailoring Cu valence and oxygen vacancy in Cu/TiO_2 catalysts for enhanced CO_2 photoreduction efficiency. *Appl. Catal. B: Environ.* **2013**, *134-135*, 349–358.

[71] Zhang, Z. Y.; Wang, Z.; Cao, S.-W.; Xue, C. Au/Pt nanoparticle-decorated TiO_2 nanofibers with plasmon-enhanced photocatalytic activities for solar-to-fuel conversion. *J. Phys. Chem. C* **2013**, *117*, 25939–25947.

[72] Tu, W. G.; Zhou, Y.; Liu, Q.; Yan, S. C.; Bao, S. S.; Wang, X. Y.; Xiao, M.; Zou, Z. G. An *in situ* simultaneous reduction-hydrolysis technique for fabrication of TiO_2-graphene 2D sandwich-like hybrid nanosheets: Graphene-promoted selectivity of photocatalytic-driven hydrogenation and coupling of CO_2 into methane and ethane. *Adv. Funct. Mater.* **2013**, *23*, 1743–1749.

[73] Zarifi, M. H.; Mohammadpour, A.; Farsinezhad, S.; Wiltshire, B. D.; Nosrati, M.; Askar, A. M.; Daneshmand, M.; Shankar, K. Time-resolved microwave photoconductivity (TRMC) using planar microwave resonators: Application to the study of long-lived charge pairs in photoexcited titania nanotube arrays. *J. Phys. Chem. C* **2015**, *119*, 14358–14365.

[74] Fàbrega, C.; Hernández-Ramírez, F.; Prades, J. D.; Jiménez-Díaz, R.; Andreu, T.; Morante, J. R. On the photoconduction properties of low resistivity TiO_2 nanotubes. *Nanotechnology* **2010**, *21*, 445703.

[75] Zou, J. P.; Zhang, Q.; Huang, K.; Marzari, N. Ultraviolet photodetectors based on anodic TiO_2 nanotube arrays. *J.*

Phys. Chem. C **2010**, *114*, 10725–10729.

[76] Liu, G. H.; Hoivik, N.; Wang, X. M.; Lu, S. S.; Wang, K. Y.; Jakobsen, H. Photoconductive, free-standing crystallized TiO_2 nanotube membranes. *Electrochim. Acta* **2013**, *93*, 80–86.

[77] Zhao, Y.; Hoivik, N.; Wang, K. Y. Photoconductivity of Au-coated TiO_2 nanotube arrays. In *Proceedings of the 14th IEEE International Conference on Nanotechnology*, Toronto, 2014, pp 180–183.

[78] Bahnemann, D. W.; Hilgendorff, M.; Memming, R. Charge carrier dynamics at TiO_2 particles: Reactivity of free and trapped holes. *J. Phys. Chem. B* **1997**, *101*, 4265–4275.

[79] Tamaki, Y.; Furube, A.; Murai, M.; Hara, K.; Katoh, R.; Tachiya, M. Direct observation of reactive trapped holes in TiO_2 undergoing photocatalytic oxidation of adsorbed alcohols: Evaluation of the reaction rates and yields. *J. Am. Chem. Soc.* **2006**, *128*, 416–417.

[80] Xi, G. C.; Ouyang, S. X.; Li, P.; Ye, J. H.; Ma, Q.; Su, N.; Bai, H.; Wang, C. Ultrathin $W_{18}O_{49}$ nanowires with diameters below 1 nm: Synthesis, near-infrared absorption, photoluminescence, and photochemical reduction of carbon dioxide. *Angew. Chem., Int. Ed.* **2012**, *51*, 2395–2399.

[81] Li, Y.; Wang, W.-N.; Zhan, Z. L.; Woo, M.-H.; Wu, C.-Y.; Biswas, P. Photocatalytic reduction of CO_2 with H_2O on mesoporous silica supported Cu/TiO_2 catalysts. *Appl. Catal. B: Environ.* **2010**, *100*, 386–392.

[82] Yang, C.-C.; Yu, Y.-H.; van der Linden, B.; Wu, J. C. S.; Mul, G. Artificial photosynthesis over crystalline TiO_2-based catalysts: Fact or fiction? *J. Am. Chem. Soc.* **2010**, *132*, 8398–8406.

[83] Liu, D.; Fernández, Y.; Ola, O.; Mackintosh, S.; Maroto-Valer, M.; Parlett, C. M. A.; Lee, A. F.; Wu, J. C. S. On the impact of Cu dispersion on CO_2 photoreduction over Cu/TiO_2. *Catal. Commun.* **2012**, *25*, 78–82.